Ab Initio studies of the interaction potential for the Xe-NO($X^2\Pi$) van der Waals complex: Bound states and fully quantum and quasi-classical scattering.

J. Kłos,[1,2,a)] F. J. Aoiz,[2,b)] M. Menéndez,[2] M. Brouard,[3,c)] H. Chadwick,[3] and C. J. Eyles[3]

[1)] *Department of Chemistry and Biochemistry, University of Maryland, College Park, MD 20742-2021 USA*

[2)] *Departamento de Química Física, Facultad de Química, Universidad Complutense, 28040 Madrid, Spain*

[3)] *The Department of Chemistry, University of Oxford, The Physical and Theoretical Chemistry Laboratory, South Parks Road, Oxford, OX1 3QZ, United Kingdom*

(Dated: Version from 11 June 2012)

Adiabatic potential energy surfaces for the ground electronic state of the Xe$\cdots$NO($X^2\Pi$) van der Waals complex have been calculated using the spin-restricted coupled cluster method with single, double and non-iterative triple excitations (RCCSD(T)). The scalar relativistic effects present in the Xe atom were included by effective core potential and we extended basis with bond functions to improve the description of the dispersion interaction. It has been found that the global minimum on the A' adiabatic surface occurs at a T-shaped geometry with $\gamma_e = 94^\circ$ and $R_e = 7.46\,a_0$, and with well depth of $D_e = 148.68\,cm^{-1}$. There is also an additional local minimum for the collinear geometry Xe-NO with a well depth of $104.5\,cm^{-1}$. The adiabat of A'' symmetry exhibits a single minimum at a distance $R_e = 7.68\,a_0$ and has a skewed geometry with $\gamma_e = 64^\circ$ and a well depth of $148.23\,cm^{-1}$. Several C_{nl} van der Waals dispersion coefficients are also estimated, of which $C_{6,0}$ and $C_{6,2}$ are in a reasonable agreement with previous theoretical results obtained by Nielson *et al.* [J. Chem. Phys. 64, 2055 (1976)]. The new potential energy surfaces were used to calculate bound states of the complex for total angular momentum quantum numbers up to $J = 7/2$. The ground state energy of Xe$\cdots$NO($X^2\Pi$) is D_0=117 cm^{-1}, which matches the experimental value very accurately (within 3.3%). Scattering calculations of integral and differential cross sections have also been performed using fully quantum close coupling calculations and quasi-classical trajectory (QCT) method at a collision energy of 63 meV. These calculations reveal the important role played by *L*–type rainbows in the scattering dynamics of the heavier Rg-NO(X) systems.

[a)]Electronic mail: jklos@umd.edu

[b)]Electronic mail: aoiz@quim.ucm.es

[c)]Electronic mail: mark.brouard@chem.ox.ac.uk

I. INTRODUCTION

Rotational energy transfer collisions of rare gases (Rg) with NO have traditionally received a great deal of attention both experimentally and theoretically to the point at which they have become prototypes of the scattering of closed shell (c–s) atoms with open shell (o–s) diatomic molecules. The NO molecule on its electronic ground state ($X^2\Pi$) is easily detectable quantum state selectively using either laser induced fluorescence[1], one-color $(1+1)^2$ or two colour $(1+1')^3$ resonance enhanced multiphoton ionization. State resolved integral (ICS) and differential cross sections have been measured for He, Ar, Ne collision with NO for spin conserving, $F_1 \rightarrow F_1$, and spin changing, $F_1 \rightarrow F_2$, transitions, where F_1 and F_2 designate the rotational manifolds that arise from the lower $^2\Pi_{1/2}$ and upper $^2\Pi_{3/2}$ states, respectively, as well as for transitions into different final Λ-doublet components[4–9].

High level *ab initio* potential energy surfaces (PES) have been produced for the Rg–NO systems over the last ten years. Currently there are accurate PESs for He+NO($X^2\Pi$)[10], Ne+NO($X^2\Pi$)[11–13], Ar+NO($X^2\Pi$)[14,15] and, more recently for Kr+NO($X^2\Pi$)[16,17]. Most of the PESs have been determined for a fixed internuclear distance of the NO molecule which is expected to be an excellent approximation for the study of rotational energy transfer at relatively low collision energies, as confirmed by the good agreement between experimental and theoretical results. However, to our knowledge, no PESs for the Xe-NO($X^2\Pi$) system have been calculated up to date. Although the very efficient cluster formation in molecular beam expansions with Xe poses serious experimental problems, this system is nonetheless important to close the gap in knowledge of the series of Rg+NO($X^2\Pi$) systems.

The presence of attractive forces, whose magnitude increases with the size of the Rg atom, makes these systems an interesting case study. Although the role of attractive forces in rotational energy transfer has received less attention than collisions dominated mainly by repulsive forces, it is known that the existence of attractive wells in the PES may give rise to "L–type" rainbows, analogous to those found in elastic scattering, which show up as maxima in the deflection function; *i.e.*, the dependence of the scattering angle on the orbital angular momentum or impact parameter[18,19]. Quantum mechanically, the occurrence of rainbows is manifested as an interference pattern at relatively small scattering angles. In addition, the presence of a sufficiently attractive well can give rise to a bulge in the opacity function at the highest orbital angular momenta corresponding to those values beyond the glory impact

parameter[20,21].

The paper is organized as follows. Section II describes the calculation of the potential energy surfaces for the Xe-NO system. The general features of the PESs are discussed in Section III, whilst Section IV presents the results of the bound state calculations for the Xe$\cdots$NO van der Waals complex. Finally, Section V describes the method used to perform the scattering calculations, and Section VI presents the scattering results. The paper concludes with a short summary of findings and conclusions.

II. *AB INITIO* CALCULATIONS OF ADIABATIC POTENTIALS

Two potential surfaces are required to describe collisions between NO($^2\Pi_{1/2,3/2}$) molecules with Rg atoms, of $^2A'$ and $^2A''$ symmetry. In the $^2A'$ state the singly occupied π^* orbital of NO(X) is located in the N-O-Rg plane, while in the second it lies perpendicular to it. To obtain the adiabatic PESs of the Xe-NO(X$^2\Pi$) van der Waals system we have used the supermolecular approach which defines the intermolecular interaction energy in the following manner:

$$\Delta E_{\rm AB}(R,\gamma) = E_{\rm AB}(R,\gamma) - E_{\rm A}^{DCBS}(R,\gamma) - E_{\rm B}^{DCBS}(R,\gamma)\,, \tag{1}$$

where R and γ are the Jacobi coordinates, defined in subsection II A, and $DCBS$ stands for the Dimer Centered Basis Set and denotes the fact that the A and B monomer calculations are performed using a basis set of the whole AB dimer. This procedure is equivalent to the counterpoise correction (CP) method of Boys and Bernardi[22]. Due to the open-shell character of the NO(X$^2\Pi$) molecule, the CP procedure is slightly more complicated than that in the closed shell case. The complications stems from the fact that the energies of the open-shell monomer in the DCBS basis must be calculated with the same orientation of the singly-occupied orbital as in the corresponding dimer belonging to the A' or A'' representation of the C_s symmetry group.

All the electronic structure calculations were performed using the MOLPRO suite of programs[23], using a similar approach as those taken for the other Rg+NO(X) PESs[10,14–17].

A. Geometries, basis sets and method

The Xe–NO(X) van der Waals complex is usually described in Jacobi coordinates. The intermolecular vector $\boldsymbol{R}$ points from the center of mass of the NO molecule towards the Xe atom. The angle γ is defined as the angle between $\boldsymbol{R}$ and diatomic vector $\boldsymbol{r}$ with $\gamma = 0°$ defining the Xe-N-O collinear arrangement. The calculations have been carried out by fixing the NO($X^2\Pi$) internuclear distance to its equilibrium value $r_e = 1.15077\,\text{Å}$[24], such that no dependence on r appears in the XeNO potential. Calculations of the adiabatic energies were carried out for 28 intermolecular distances in the range between 2.75 Å and 25 Å, whilst the angular grid for the γ variable consisted of 7 values (every 30°).

The calculations were performed in the basis set composed of augmented, correlation-consistent triple zeta basis set of Dunning *et al.*[25,26] (denoted as aug-cc-pvtz) for the NO molecule, and an effective core potential (ECP) of the Stuttgart/Cologne group from the MOLPRO program library for the Xe atom. The ECP46MWB effective core potential was chosen to describe 46 inner electrons and account for scalar relativistic effects. This basis set was augmented with the set of bond functions[27] [$3s3p2d1f1g$] placed in the middle of the distance R to improve description of the dispersion component of the interaction. The bond functions had the following exponents: sp, 0.9, 0.3, 0.1; d, 0.6, 0.2; and fg, 0.3.

The spin-restricted Hartree-Fock (RHF) molecular orbitals suited as a reference orbitals for subsequent spin-restricted coupled cluster calculations with single, double and non-iterative triple excitations (RCCSD(T))[28,29]. This method ensured that there was no spin contamination.

B. Expansion and fitting of diabatic potentials

The form of a potential expansion for a diatomic molecule in a $^2\Pi$ state interacting with an ^1S state atom was first given by Alexander[30]. For the purpose of the bound state and scattering calculations, it is convenient to use the diabatic potentials obtained in the transformation from a real p-orbital basis to a Λ-signed basis, where Λ is the projection quantum number of the singly occupied p-electron. The diabatic surfaces, V_{sum} and V_{diff},

are constructed as the half sum and half difference of the A'' and A' adiabats, respectively:

$$V_{\rm sum}(R,\gamma) = \frac{1}{2}\left[V_{A''}(R,\gamma) + V_{A'}(R,\gamma)\right] = \sum_{l=0}^{10} V_{l0}(R) d^l_{00}(\gamma)\,, \tag{2}$$

$$V_{\rm diff}(R,\gamma) = \frac{1}{2}\left[V_{A''}(R,\gamma) - V_{A'}(R,\gamma)\right] = \sum_{l=2}^{10} V_{l2}(R) d^l_{20}(\gamma)\,.$$

The $V_{\rm sum}$ and $V_{\rm diff}$ diabatic PES's are expanded in reduced rotation matrix elements of order $m = 0$ and $m = 2$ to maximum $l = 10$, respectively[30] which for one of the subindexes equal to zero are related in a simple way to spherical harmonics and to the associated Legendre functions[31,32]:

$$d^l_{m0}(\gamma) = \left(\frac{4\pi}{2l+1}\right)^{1/2} Y_{lm}(\gamma, 0) = (-1)^m \sqrt{\frac{(l-m)!}{(l+m)!}} P^m_l\left(\cos\gamma\right) \tag{3}$$

Alexander has shown that within the Hund's case (a) coupling scheme, spin-orbit (SO) conserving transitions take place on the summed potential, $V_{\rm sum}$, whilst spin-orbit changing collisions take place on the difference potential $V_{\rm diff}$[33].

In practice, the *ab initio* points for the A' and A'' PES's were fit separately in a two-step procedure. First, for each value of γ, the R-dependence was fit by a variant of the functions introduced by Degli-Esposti and Werner[34],

$$V(R) = G(R)\,{\rm e}^{-a_1 R - a_2} - T(R)\sum_{n=6}^{9} C_n R^{-n}, \tag{4}$$

where

$$G(R) = \sum_{j=0}^{8} g_j R^j \tag{5}$$

and

$$T(R) = 1/2\left[1 + \tanh(1 + tR)\right]\,. \tag{6}$$

The parameters a_1, a_2, g_j, t, and the long-range coefficients C_n were optimized for each value of γ, separately, by use of a modified Levenberg-Marquardt algorithm for the non-linear variables and a standard least-squares fit for the linear variables.

For each desired value of R_i and γ_i, Eq. (4) was then used to generate the values of $V_{A'}$ and $V_{A''}$ on the γ grid. From these the values of $V_{\rm sum}$ and $V_{\rm diff}$ were obtained from Eq. (2). Finally, the values of the expansion coefficients $V_{l0}(R_i)$ and $V_{l2}(R_i)$ were obtained by solution of sets of linear equations.

Both the $V_{\rm sum}$ diabat and the A' adiabat exhibit near-homonuclear symmetry with respect to $\gamma = 90°$, similar to what has been observed in the case of Kr-NO[17]. The two-lobed shape of the difference potential, $V_{\rm diff}$, is typical for NO(X) interacting with a spherical target, similar to He–NO(X)[10]. In Fig. 1, we show plots of the radial expansion coefficients of the sum and difference diabats, respectively. Because of the near-homonuclear symmetry, the expansion coefficient with $l = 2$ for $V_{\rm sum}$ and $l = 4$ for $V_{\rm diff}$ are slightly larger than those with l odd.

C. $C_{n,l}$ dispersion coefficients

We have also estimated van der Waals dispersion coefficients $C_{n,l}$ of the expansion of the long range potential, $V_{\rm lr}(R,\gamma)$, as

$$V_{\rm lr}(R,\gamma) = -\sum_{n=6}^{N_{max}} \sum_{l} \frac{C_{n,l}}{R^n} P_l(\cos\gamma)\,. \tag{7}$$

This has been achieved by using a linear fit of the long range values of the corresponding radial expansion coefficients of the $V_{\rm sum}$ diabat with a given l to the above expansion. The results are shown in Table I. We can compare isotropic van der Waals $C_{6,0}$ coefficient and the first anisotropic $C_{6,2}$ term with previous theoretical results obtained by Nielson *et al.*[35]. Both theoretical results are similar, taking into account error bars shown by Nielson *et al.*

III. FEATURES OF POTENTIAL ENERGY SURFACES

The stationary points of adiabatic and diabatic Xe-NO(X) PES are given in Table II, whilst contour plots of the adiabatic potentials are shown in Fig. 2. The surface of A' symmetry, shown in panel (a), exhibits three stationary points: two local collinear minima and a T-shaped global minimum. The global minimum of the A' surface is located at $\gamma_{\rm e} = 94°$ and $R_{\rm e} = 7.46\,{\rm a_0}$ with a well depth of $148.68\,{\rm cm^{-1}}$. The anisotropy of the A' surface resembles that of the A' surfaces of the He$\cdots$NO[10] and Ar$\cdots$NO systems[14,15]. In the case of He, the T-shaped minimum is more skewed towards the O-end of the NO moiety ($\gamma_{\rm e} = 100.3°$ from Ref.[10]), but, in the cases of Ar and Xe, the global minimum is around 95° (95.2° for Ar from Ref.[14]). The well depths of the local collinear minima are similar, being $104.5\,{\rm cm^{-1}}$ deep for the Xe$\cdots$N-O arrangement and $107.2\,{\rm cm^{-1}}$ for the Xe$\cdots$ON configuration. In the case of

the A' surface there is barrier of $\approx 48\,\mathrm{cm}^{-1}$ for rotation between the T-shape and the linear minima.

The A'' surface shown in the panel (b) has only one minimum at a skewed geometry located with $\gamma_e = 64^\circ$ and $R_e = 7.68\,a_0$ and a well depth of $148.2\,\mathrm{cm}^{-1}$. Collinear arrangements have saddle points instead of the minima observed on the A' surface. Again, the qualitative similarities of the A'' surface anisotropy to the cases of He, Ar, and Kr interacting with NO are noteworthy.

The contour plots of the diabatic surfaces are shown in Fig. 3. The V_{sum} diabat (panel (a)) has a single minimum with a T-shaped geometry at $\gamma_e = 90^\circ$ and $R_e = 7.52\,a_0$, and with the well depth of $141.7\,\mathrm{cm}^{-1}$. The anisotropy of this diabat shows near-homonuclear character: the surface is qualitatively symmetric with respect to $\gamma = 90^\circ$. The difference diabat V_{diff} shown in panel (b) of Fig. 3 is mostly responsible for the spin-orbit changing transitions, and its anisotropy is similar to the case of the other rare gas complexes with NO(X). It exhibits two attractive lobes divided by a small repulsive region corresponding to the node of the π^* molecular orbital of the NO molecule.

IV. BOUND STATES CALCULATIONS

The variational fully quantum close-coupling (CC) calculations of bound states were performed using diabatic surfaces developed in this work. We used the HIBRIDON[36] suite of programs designed for scattering and bound state calculations on many types of collisional systems. In these CC bound state calculations the open-shell electronic structure of the NO molecule was taken into account. Following the work of Alexander[14,15], the rotational levels of the NO molecule are described in the Hund's case (a) basis:

$$|\Lambda\Sigma\, j\, m\, \omega\, \epsilon\rangle = 2^{-1/2}\Big[\, |j\, m\, \omega\rangle|\Lambda\, \Sigma\rangle \,+\, \epsilon|j\, m\, -\omega\rangle\, |-\Lambda-\Sigma\rangle\, \Big]\,. \tag{8}$$

Here j stands for angular momentum quantum number of the diatomic molecule. ω and m are projections of the angular momentum $\boldsymbol{j}$ along molecule and space-fixed z-axes, respectively. The ket $|\Lambda\Sigma\rangle$ describes the electronic component of wave function of the diatomic. Λ is molecule-fixed projection of electronic orbital angular momentum and Σ is the spin angular momentum projection, also in the molecule-fixed frame. The ϵ index distinguishes the e and f spectroscopically labeled levels, which have $\epsilon = +1$ and $\epsilon = -1$, respectively. The total parity of the wave functions is $p = \epsilon(-1)^{j-1/2}$.

The radial part of the wave functions in the bound-state calculations is expanded in a replicated Gaussian basis[37] distributed between R=4.5 a_0 and 12 a_0 with a step of 0.5 a_0. This gives a total of 16 radial basis functions. The angular basis was set to run up to $j_{\max} = 10.5$. We used the following molecular constants of the NO($X^2\Pi$) molecule: the rotational constant $B_0 = 1.69611\,\mathrm{cm}^{-1}$[24], the spin-orbit coupling constant $A = 123.1393\,\mathrm{cm}^{-1}$, and Λ-doubling parameters $p = 1.172 \times 10^{-2}\,\mathrm{cm}^{-1}$, $q = 6.7 \times 10^{-4}\,\mathrm{cm}^{-1}$. The reduced mass of Xe-NO was set to 24.4398 a.m.u. The bound states were calculated for both values of the total parity and for the total angular momentum quantum number up to $J = \frac{7}{2}$. The CC results for the lowest 14 bound states for $J = 1/2$ and $J = 3/2$ are shown in Table III. The calculated zero-point corrected dissociation energy is $117\,\mathrm{cm}^{-1}$. This is 4 cm^{-1} shallower than the experimental estimate of $121\,\mathrm{cm}^{-1}$ by Gamblin *et al.*[38]. This results in the relative error of 3.3 % with respect to the experimental value. We attribute part of this error to the incompleteness of the basis set used in the *ab initio* calculations and another part in the fact that we use 2-dimensional PES with the NO geometry fixed at equilibrium value. The inclusion of the NO bond stretching could increase the value of the D_0 up to some degree which would bring it to a closer agreement with the experimental value.

In the recent work of Kłos *et al.*[11] on rare gas complexes with the NO($A^2\Sigma^+$) molecule there is the table of theoretical and experimental zero-point corrected dissociation energies for both the NO($A^2\Sigma^+$) and NO($X^2\Pi$) molecules that includes the result for the Xe atom calculated in the present work.

The bound states in Table III are characterized by the number of radial n_s and angular n_b nodes in the corresponding wave function. States are also labeled with the P quantum number which is the projection of the total angular momentum J on the z-axis of the molecular frame. As one can notice, the parity splitting is on the order of 0.04 cm^{-1} for the ground ro-vibrational state. The first excited van der Waals stretch frequency ω_1 is around 21.5 cm^{-1}. More detailed analysis of the Xe-NO bound states and new experimental measurement of the Xe-NO spectrum is currently ongoing and will be reported elsewhere[39].

V. QCT AND QM SCATTERING CALCULATIONS

A. Quasi-classical trajectory calculation method

The quasiclassical trajectory (QCT) methodology is essentially the same as used in previous work on Ar–NO($X^2\Pi$)[20,21,40] inelastic collisions. We will report only those particular details that are pertinent to this work. Batches of 5×10^5 trajectories were calculated on the $V_{\rm sum}$ PES presented in this study at a collision energy $E_{\rm col}$=508 cm^{-1} (equivalent to 63 meV) for each of the NO initial rotational levels j=0, 2, 5, 8, 11 and 14. This number of trajectories ensured proper statistics and convergence of integral and differential cross sections and the opacity functions. As noted above, in Hund's case (a), the $V_{\rm sum}$ potential governs rotational transitions within a given spin-orbit manifold (in this case $\Omega = 1/2$). Since the potential has been calculated only for NO fixed at its equilibrium internuclear distance, $r_{\rm e}$, we use the method of Lagrange multipliers to force a rigid rotor constraint ($r = r_{\rm e}$) in the integration of the classical equations of motion[41].

To assign the initial and final rotational states, the square of the rotational angular momentum was equated to $j(j+1)\hbar^2$. In the case of the final rotational state, the resulting value was rounded to the nearest integer. A trajectory was deemed inelastic when the absolute value of the difference between the final and initial rotational quantum numbers $|\Delta j| = |j'-j|$ was greater than 0.5. The only exception to this was when the initial rotational quantum number was j=0. In this case, only trajectories leading to j' in the [1.0, 1.5] range were assigned to the first excited rotational state j'=1. This somewhat arbitrary criterion is based on the rationale that considers that the range $j' \in [0, 0.5]$ is smaller than any interval corresponding to any other rotationally excited state. Ultimately, this criterion is justified by the comparison with either closed-shell (c–s) or open-shell (o–s) QM results. Alternatively, the quantization $(j' + 1/2)^2\hbar^2$ was also used to assign the final rotational states. For $\Delta j = \pm1$ the agreement between QM and QCT ICS is slightly better, but for the remaining Δj transitions the difference between the results using these different types of quantization was negligible.

To determine the value of the maximum impact parameter, $b_{\rm max}$, used in the calculations, the change in rotational quantum number was monitored. The impact parameter was increased until no trajectories leading to $|\Delta j| > 0.5$ were found. The values of $b_{\rm max}$

ranged from 8 Å for j=0 to 5.5 Å for j=14. With these values, approximately 50% of the trajectories were assigned to inelastic collisions. The inelastic collision probabilities, $P(J)$, were calculated by the method of moment expansion in Legendre polynomials as detailed in Appendix C of ref. 42. Notice that $P(J)$ are functions of the total angular momentum quantum number, J, and except for j=0, they are not the same as the actual opacity functions as a function of the orbital angular momentum, $P(\ell)$, or those as a function of the impact parameter $P(b)$, especially for J (ℓ) values comparable to j.

The solid angle differential cross sections, $\mathrm{d}\sigma/\mathrm{d}\omega$, were also calculated by the method of moment expansion in Legendre polynomials. To determine the scattering angle differential cross sections, $\mathrm{d}\sigma/\mathrm{d}\theta = 2\pi \sin\theta \, \mathrm{d}\sigma/\mathrm{d}\omega$, an expansion in sine Fourier series was used.

B. Fully quantum close coupling scattering method

Open–shell (o–s) and closed–shell (c–s) QM calculations were carried out with the close coupling (CC) method. The o–s QM scattering calculations were performed at a collision energy of 63 meV with respect to ground spin-orbit ($\Omega = 1/2$) and for the e Λ-doublet level of the initial rotational states $j = 1/2, 5/2, 11/2, 17/2$, 23/2 and 29/2. The c–s QM calculations were carried out at the same collision energy for the initial rotational states $j = 0, 2, 5, 8, 11$, and 14. These two calculations were performed using the V_{sum} diabatic PES, therefore treating approximately the NO(X) molecule as a closed shell species.

The state-resolved opacity functions in the case of the o–s QM and c–s QM approaches can be calculated in the following way[42,43] from the S-matrix elements:

$$P_{j\alpha\to j'\alpha'}(J) = \frac{1}{(2\min(J,j)+1)} \sum_{\ell=|J-j|}^{J+j} \sum_{\ell'} \left| S^J_{j'\alpha'\ell',j\alpha\ell} \right|^2 , \tag{9}$$

or from the partial cross sections:

$$P_{j\alpha\to j'\alpha'}(J) = \frac{k^2}{\pi} \frac{2j+1}{(2J+1)(2\min(J,j)+1)} \sigma^J_{j'\alpha',j\alpha} , \tag{10}$$

where the total angular momentum quantum number, J, is half-integer in the case of the o–s QM treatment, and ℓ (ℓ') is the initial (final) orbital angular momentum quantum number. α denotes the set of additional indices characterizing the quantum state (*i.e.* the Λ-doublet level). $S^J_{j'\alpha'\ell',j\alpha\ell}$ refers to the S-matrix element for transition between initial rotational quantum number j and final j', expressed in the space-fixed orbital angular momentum

representation. In order to compare the o–s QM opacity function with those obtained by c–s QM and QCT calculations, the opacity functions, $P_j^{\Delta\Omega=0}(J)$, for spin–orbit conserving, $F_1 \rightarrow F_1$, and $P_j^{\Delta\Omega=1}(J)$ for spin–orbit changing, $F_1 \rightarrow F_2$, transitions were added. The total inelastic probability as a function of J (the opacity function) was summed over final rotational states.

In addition, since the o–s QM transition for each Δj and $\Delta\Omega$ corresponds to four distinct Λ-doublet resolved transitions ($e \rightarrow e$, $f \rightarrow f$, $e \rightarrow f$, and $f \rightarrow e$), we assume that the QCT and c–s QM opacity functions, and integral and differential cross sections, should be compared with the sum over the two final Λ-doublet levels and the averaged over the two initial Λ-doublet levels of the o–s QM quantities, for both SO conserving and SO changing transitions. Specifically, for $j \rightarrow j'$ integral cross sections, $\sigma(\Delta j)$, the expression is given by

$$\sigma^{\mathrm{QCT}}(\Delta j) \approx \frac{1}{2} \sum_{\Omega'} \sum_{\epsilon,\epsilon'} \sigma^{\mathrm{QM}}(j, \epsilon, \Omega \rightarrow j', \epsilon', \Omega') \,, \tag{11}$$

where ϵ is the parity (Λ-doublet) index. The analogous equations were applied to compare differential cross sections and final state-resolved partial opacity functions between QCT, c–s QM and o–s QM methods.

In the QM calculations the set of close coupling equations[44] was propagated numerically using the hybrid propagator of Manolopoulos and Alexander[45,46] with a maximum of the total angular momentum quantum number, J, set between 200 to 300 for convergence. The Hamiltonian of the system was diagonalized using a rotational basis consisting of 20 functions of the NO molecule. The molecular parameters of the NO were kept the same as described in Section IV. The propagation was performed from $5.0\,\mathrm{a_0}$ to $35\,\mathrm{a_0}$ with a step of $0.1\,\mathrm{a_0}$. For both the o–s QM and c–s QM calculations the HIBRIDON[36] suite of codes was used.

VI. SCATTERING RESULTS

A. Integral cross sections

The integral cross sections (ICS) at E_{col}=63 meV from the initial state j=1/2 (j=0 for the c–s QM and QCT data) are represented in Fig. 4. The c–s QM ICSs show oscillations that are not present in either the o–s QM results once averaged over Λ–doublet transitions or in the

QCT results. This oscillatory structure, which is more pronounced at low Δj values, arises from the dominance of even terms in the Legendre expansion of the internuclear molecule that reflects the near–homonuclear character of the NO molecule. This effect was discussed and explained within the framework of a semiclassical model by McCurdy and Miller[47] as an interference effect originating from scattering from either end of the molecule. At low Δj values, ≤ 6, the parity conserving (Δj even) transitions exhibit larger cross sections than those for parity breaking transitions (Δj odd), whilst the opposite occurs for $\Delta j > 8$.

The agreement between the three sets of calculations is fairly good, especially between the o–s QM and QCT results. It should be borne in mind that the QCT cross section for Δj=1 have been calculated neglecting those trajectories whose (real) rotational product quantum number was below j=1. The cross sections for the XeNO(X) system at the same collision energy are larger than for other Rg+NO(X) processes, most notably as compared to He+NO(X) and to a lesser extent Ar+NO(X).

The o–s QM ICSs from the lowest initial j=0.5, $\Omega = 1/2$ and e Λ–doublet state into Ω=1/2 (F_1) and Ω=3/2 (F_2) final states are represented in the top and bottom panels of Fig. 5, respectively, and in Table IV. The ICSs are also resolved into their final Λ-doublet component. As might be expected, the oscillations that were averaged out by summing over the two Λ-doublet components show up clearly when the parity conserving and parity breaking transitions are resolved. The cross sections for $e \rightarrow e$ and even Δj transitions are considerably higher than those for odd Δj, and the opposite takes place for $e \rightarrow f$ transitions. Only for $\Delta j > 8$, is the interference quenched and the cross section become more similar. This effect is even more pronounced for spin changing collisions. In contrast to the collisions of He+NO(X), the ICSs for low j' states are on average larger than those for higher j' values. The $F_1 \rightarrow F_2$ transitions are weaker by almost an order of magnitude than the corresponding spin conserving transitions for all Δj. The oscillations are even sharper than for the spin conserving–transitions and until Δj=8, parity conserving (even parity) transitions are much more intense than those implying parity breaking (odd parity).

The QCT, c–s QM and o–s QM rotational energy transfer cross sections from various initial rotational states are represented in Fig. 6. Once more the o–s QM ICSs are the result of averaging over the initial e and f states and summing over final Ω=0, 1 and Λ-doublet components. The agreement between the three sets of calculations is very good. Only for $\Delta j = \pm 1$ the QCT results are appreciable higher that those obtained with the QM

approaches. Oscillations in the c–s QM ICSs are also present, but they are less pronounced than those found for the transitions from the ground rotational state. The curves display a clear asymmetry, with $\Delta j > 0$ transitions being favored for initial states with initial j=2 and 5, and $\Delta j < 0$ transitions preferred for the initial state j=14.

B. Opacity functions

In a previous study on the inelastic collisions of Ar+NO(X) the calculations revealed the presence of an "L–type" or impact parameter rainbow, analogous to those appearing in elastic scattering, that cause a maximum in the deflection function[20]. This 'orientational' rainbow[18,48,49] is clearly manifest in the opacity function as a separate lobe at the highest impact parameters. This structure was also confirmed in QM calculations and can be traced back to the competition of scattering dominated by attractive and repulsive forces. Given the fact that XeNO(X) exhibits a somewhat deeper potential energy well compared with that found for the ArNO(X) system, one would expect similar behavior in the heavier system of current focus.

Fig. 7 clearly shows that this is indeed the case. In this figure the total opacity function, *i.e.*, the total probability for inelastic collisions as a function of the total angular momentum, J, is shown for the QCT, c–s QM and o–s QM calculations at a collision energy of 63 meV. Note that in this case the total angular momentum is equivalent to the orbital angular momentum, since the initial rotational angular momentum of the NO(X) is either $j = 0.5$ in the o–s QM calculations (a negligible value considering the magnitude of the orbital and total angular momenta involved), or 0 in the c–s QM and QCT calculations. There is generally excellent agreement between the three theoretical treatments, although the o–s QM calculations show a slightly reduced probability at high J compared with the c–s QM and QCT results. The latter results are, however, in very good accord with each other. For total angular momentum quantum numbers, J, below ∼110, corresponding to $b \simeq 4.5$Å, the opacity functions from each set of calculations show a near constant value of around 0.9. The probability above $J \approx 110$ first shows a cleft with a minimum at $J \approx 125$ (b=4.7 Å) and then a maximum, reaching around 0.7 at $J \simeq 140$ (equivalent to $b \approx 5.0$Å) and then decrease slowly until $J \approx 200$. As discussed further below, this L–type orientational rainbow feature can be clearly associated with the maximum in the classical deflection function. The results

shown in Fig. 7 are typical of inelastic scattering in the presence of a significant attractive well, as discussed by Schinke *et al.*[18] and by Mayne and Keil[19] for model systems.

In the bottom panel of Fig. 7 the summed over j' opacity function corresponding to o–s QM calculations is shown resolved in the final SO-manifolds with $\Omega' = 1/2$ (F_1) (brown dot–dot-dash line) and $\Omega' = 3/2$ (F_2) (short-dash blue line). These to quantities summed up will form the total o–s QM opacity function presented by red dashed line in this figure. As can be seen, the bulge associated to rainbow scattering is completely absent in the $F_1 \rightarrow F_2$ opacity function that comprises only total angular momenta $J \leq 110$ and becomes zero in coincidence with the minimum of the $F_1 \rightarrow F_1$ opacity function assigned to the inelastic glory impact parameter (see below).

When the opacity functions are resolved in final states, it becomes clear that the *L*-type rainbow only appears for low Δj transitions; those which require less momentum transfer. Fig. 8 depicts the c–s QM j' resolved opacity functions corresponding to odd Δj (parity changing) transitions. The behavior for Δj (parity conserving) transitions is very similar and follows the same pattern. The arrows in the various $P(J)$ indicate the minimum corresponding to the cleft in the opacity function of Fig. 7 that appears at J=123 for all these transitions. For a narrow range of orbital angular momenta around this value, little or none rotational excitation takes place at the collision energy considered. The bulge associated to rainbow scattering at higher values diminishes rapidly as Δj increases, and for Δj=7 has practically vanished. These higher Δj transitions are dominated by the repulsive part of the potential and take place at increasingly smaller impact parameters, hence these transitions will be similar to those taking place in systems with shallower or well. In turn, the lowest Δj transitions can be considered as quasi-elastic with the anisotropic attractive potential dominating the collision. Interestingly, calculations carried out suppressing the attractive part of the potential (simply making $V_{\rm sum}(R, \gamma) = 0$ whenever it has a negative value) causes the complete disappearance of the bulge for all the transitions and the retreat of the opacity function to smaller J values. This effect was also found in semiclassical calculations by Barrett *et al.*[48] and more recently in the case of inelastic collisions of Cl + H_2[50,51].

In Fig. 9 we compare the total opacity functions from the c–s QM calculations for the complete series of NO(X) collisions with the rare gases, He through to Xe. The initial rotational state is $j = 0$ and the collision energy is 63 meV. These data emphasize the

increasing presence of L–type rainbow structure in the total opacity functions with increasing rare gas atomic number, reflecting the varying role played by attractive forces in the series of Rg-NO(X) species. Attractive forces are practically absent in the potential for He-NO(X), and the L–type rainbow feature is barely visible in the total opacity function. On the other hand, very significant L–type structure is observed for Kr-NO(X) and Xe-NO(X), reflecting the importance of attractive forces in these scattering encounters. Note that the heights and shapes of the L–type orientational rainbows in Kr-NO(X) and Xe-NO(X) are rather similar, reflecting the similarities in their PESs and in particular of their respective well depths. In fact, the maximum of the rainbow appears in both cases at the same impact parameter and the different in the value of the total angular momentum is just due to the difference in their reduced masses.

The total opacity functions, $P(J;j)$, from the QCT, o–s QM, and c–s QM calculations are presented in Fig. 10, for a series of initial rotational states, j. Each of the three sets of calculations show very similar qualitative behavior, although, as with the data shown in Fig. 7 for initial $j = 0.5$, the o–s QM data possess slightly less pronounced outer maxima in probability. L–type rainbows are generally observed at low initial j, and practically disappear for $j \geq 8$. One reason for this is that the anisotropy of the potential is more effectively averaged as j increases, and thus the effects of the attractive wells are less pronounced. Rotational transitions between excited rotational states imply higher radial energy and therefore smaller impact parameters Furthermore, however, rotational inelastic scattering requires a more impulsive encounter as j increases, since a given Δj transition at high initial j requires the transfer of more energy than one at low j and this implies a progressive decrease of the maximum value of the impact parameter.

C. Differential cross sections

The manifestation of L–type rainbows are also ubiquitous in the total and quantum state resolved differential cross sections. Panel (a) of Fig. 11 shows the classical deflection function, the dependence of the scattering angle on impact parameter, for initial $j = 0$. A strong correlation is found between scattering angle and initial impact parameter: the figure has a strong resemblance to that found in atom-atom elastic scattering. As noted above, similar behavior has also been observed in the case of inelastic scattering of NO(X)

by Ar[20] and in previous studies[48]. The outer maximum in the deflection function, which occurs at $b \simeq 5\,\text{Å}$, coincides precisely with the outer lobe in the total opacity function. Above the glory impact parameter ($b_g \approx 4.2\,\text{Å}$, for which $\theta_g = 0$), negative deflection angles dominate, and the trajectories are mainly far-side in nature. Beyond the outer maximum in the deflection function trajectories principally sample the attractive limb of the potential, but as b decreases below $\approx 5\,\text{Å}$ the repulsive part of the potential plays an increasingly important role until the glory impact parameter reached, at which point there is a perfect balance between the effects of the attractive and repulsive forces and no net deflection is observed.

Panel (b) of Fig. 11 presents the total differential cross section, for each of the three theoretical approaches employed. Note the logarithmic scale used for the y-axis. The total DCS is very strongly forward scattered, reflecting the dominant role played by high impact parameter collisions which lead to relatively small deflections, and which preferentially sample attractive regions of the potential. At scattering angles around 30° the total QCT DCS shows a hint of a classical rainbow, mirroring the outer maximum in the total deflection function shown in panel (a). In this scattering angle region, the corresponding o–s QM and c–s QM data show oscillations reflecting rainbow interference between multiple pathways leading to the same scattering outcome. Overall there is excellent agreement between the o–s QM, the c–s QM, and the QCT data.

Figs. 12 and 13 provide a comparison of the DCSs resolved into different Δj transitions, starting from initial $j = 0.5$ and 14.5, respectively. Results are presented for the QCT and o–s QM calculations, with the latter appropriately summed over SO and averaged/summed over Λ-doublet transitions. The data are plotted in the form of scattering angle differential cross sections, $\mathrm{d}\sigma/\mathrm{d}\theta$, *i.e.* the solid angle DCSs weighted by $2\pi \sin\theta$, so that the plots are less dominated by forward scattering. The DCSs for $j = 0.5$ (or $j = 0$ in the QCT case) show clear rainbow peaks at low Δj, which in the o–s QM calculations are manifest as strong oscillations in the forward scattered region. These structures become less pronounced towards high Δj, although they are still observable for $\Delta j = 8$ (see Fig. 12). In contrast, the DCSs for collisions starting from $j = 14.5$, shown in Fig. 13, do not display any clear evidence of rainbow structure, as would be expected on the basis of the opacity function data shown in Fig. 10. Overall, there is reasonable agreement between the averaged o–s QM and the QCT DCS results, although somewhat surprisingly the agreement is slightly worse

in the case of the DCSs for initial $j = 14.5$ compared with initial $j = 0.5$.

Fully Λ-doublet resolved o–s QM DCSs are shown in Fig. 14, where they are again weighted by $2\pi \sin\theta$. The initial state is $\Omega = 1/2, j = 0.5, e$. Spin-orbit conserving transitions are shown in the upper four panels, while spin-orbit changing transitions are shown in the lower four panels for the same Δj and Λ-doublet changing collisions. The data are plotted in 'parity pairs'[7–9,21,40]; that is, the DCSs corresponding to transitions with the same value of $n = j' - \varepsilon\varepsilon'/2$ are plotted in the same panel. DCSs with total NO parity changing transitions shown in the left panels and total parity conserving in the right panels. It has been shown elsewhere[40,52] that within a Hund's case (a) coupling scheme, transitions to adjacent j' levels of the same parity form pairs of transitions which are coupled by the same terms in the expansion of the potential, and therefore tend to be similar in magnitude and scattering angle dependence. This behavior is clearly reproduced here for collisions of Xe with NO(X) for both spin-orbit conserving and changing collisions. In general, the total NO parity conserving transitions tend to have greater amplitude in the sideways and backward directions than the parity changing collisions, consistent with the latter being controlled by more attractive terms in the PES. There is a general tendency, particularly for the spin-orbit conserving transitions at moderate Δj, for the total NO parity conserving transitions to show a more pronounced double-peaked structure in the sideways scattering region than in the case of the parity changing collisions. Similar behavior has been found experimentally for NO(X) + Ar, and explained in terms of an NO parity-dependent interference effect[8,9,21]. It is interesting to note that this behavior is also observed here for the NO(X) + Xe system. The multiple peaked structure is less obvious in the spin-orbit changing collisions, but recall that these cross sections are an order of magnitude smaller than those for the spin-orbit conserving transitions.

Apart from these parity dependent structures, however, a key point to emphasize based on the parity resolved DCSs shown in Fig. 14 is the presence of strong rainbow interference structure at low Δj, which reflects the L–type rainbow features in the opacity functions shown in Figs. 7 and 10.

VII. SUMMARY AND CONCLUSIONS

In this work we have presented new electronic structure, bound state, and inelastic scattering calculations on the NO($X^2\Pi$)–Xe system. High-level intermolecular potential energy surface calculations have been performed for the lowest A' and A'' states of the Xe$\cdots$NO($X^2\Pi$) van der Waals complex. It is shown that the global minimum on the A' adiabatic surface occurs at a T-shaped geometry and has a well depth of $D_e = 148.68\,cm^{-1}$. The adiabat of A'' symmetry exhibits a single minimum at a skewed geometry with a well depth of $148.23\,cm^{-1}$. The new potential energy surfaces were used to calculate bound states of the Xe$\cdots$NO($X^2\Pi$) complex, thereby enabling a prediction to be made of the ground state dissociation energy of the complex, D_0=$117\,cm^{-1}$.

Scattering calculations of integral and differential cross sections have also been performed using full open–shell (o–s) and closed–shell (c–s) CC QM and QCT methods at a collision energy of 63 meV. The QM and QCT results are generally in good agreement, and reveal the important role played by L–type rainbows in the scattering dynamics, particularly for low initial rotational states of NO(X), and for transitions involving low Δj. L–type rainbows are shown to play an increasing role in the dynamics of the Rg-NO(X) systems with increasing rare gas atomic number, reflecting the varying role played by attractive forces in the series of Rg-NO(X) species. Attractive forces play a negligible role for He-NO(X), and the L–type rainbow feature is barely visible in the total opacity function. On the other hand, very significant L–type structure is observed for Kr-NO(X) and Xe-NO(X), reflecting the importance of attractive forces in these scattering encounters. With increasing rotational excitation the rainbow structures disappear due to the requirements of shorter impact parameters and to the effective average of the potential anisotropy diminishing the effects of the attractive forces. Future experiments capable of measuring fully state–to–state DCS, similar to those recently carried for Ar+NO inelastic collisions, will be most useful to determine the accuracy of the present potential and most especially of the attractive part of the PES.

Further detailed comparisons between the Rg-NO(X) systems will be presented in a future publication.

ACKNOWLEDGMENTS

The support of the Spanish Ministry of Science and Innovation (to F.J.A. and M.M. *via* grants CTQ2008-02578/BQU and CSD2009-00038) and of the UK EPSRC (to M.B. *via* Programme Grant No. EP/G00224X/1), the EU (to M.B. *via* FP7 EU People ITN project 238671), and are gratefully acknowledged. J.K. acknowledges financial support from the US National Science Foundation (grant No. CHE-0848110 to Professor M.H. Alexander) and the University Complutense de Madrid/Grupo Santander (under the "Movilidad de Investigadores Extranjeros" programme). We are grateful to Pablo Jambrina for help in some of the calculations.

REFERENCES

[1]J. D. Bradshaw, M. O. Rodgers, and D. D. Davis, Applied Optics **21**, 2493 (1982).

[2]H. Zacharias, J. B. Halpern, and K. H. Welge, Chem. Phys. Lett. **43**, 41 (1976).

[3]M. Hippler and J. Pfab, Chem. Phys. Lett. **243**, 500 (1995).

[4]H. Joswig, P. Andresen, and R.Schinke, J. Chem. Phys. **85**, 1904 (1986).

[5]H. Meyer, J. Chem. Phys. **102**, 3151 (1995).

[6]M. S. Westley, K. T. Lorenz, D. W. Chandler, and P. L. Houston, J. Chem. Phys. **114**, 2669 (2001).

[7]A. Gijsbertsen, H. Linnartz, G. Rus, A. E. Wiskerke, S. Stolte, D. W. Chandler, and K. J, J. Chem. Phys. **123**, 224305 (2005).

[8]C. J. Eyles, M. Brouard, C.-H. Yang, J. Kłos, F. J. Aoiz, A. Gijsbertsen, A. E. Wiskerke, and S. Stolte, Nat. Chem. **3**, 597 (2012).

[9]C. J. Eyles, M. Brouard, H. Chadwick, B. Hornung, B. Nichols, C.-H. Yang, J. Kłos, F. J. Aoiz, A. Gijsbertsen, A. E. Wiskerke, and S. Stolte, Phys. Chem. Chem. Phys. **14**, 5403 (2012).

[10]J. Kłos, G. Chałasiński, M. T. Berry, R. Bukowski, and S. M. Cybulski, J. Chem. Phys. **112**, 2195 (2000).

[11]J. Kłos, M. H. Alexander, R. Hernández-Lamoneda, and T. G. Wright, J. Chem. Phys. **129**, 244303 (2008).

[12]Y. Sumiyoshi and Y. Endo, J. Phys. Chem. A **114**, 4798 (2010).

[13]J. Kłos, M. H. Alexander, and H. Meyer, "New 3d potential for ne-no(x) van der waals system: Bound states and differential cross sections," Unpublished.

[14]M. H. Alexander, J. Chem. Phys. **111**, 7426 (1999).

[15]M. Alexander, J. Chem. Phys. **111**, 7435 (1999).

[16]J. C. Castro-Palacios, J. Rubayo-Soneira, K. Ishii, and K. Yamashita, J. Chem. Phys. **126**, 134315 (2007).

[17]B. Wen, H. Meyer, J. Kłos, and M. H. Alexander, The Journal of Physical Chemistry A **113**, 7366 (2009).

[18]R. Schinke, H.-J. Korsch, and D. Poppe, J. Chem. Phys. **77**, 6005 (1982).

[19]H. R. Mayne and M. Keil, J. Phys. Chem. **88**, 883 (1984).

[20]F. J. Aoiz, J. E. Verdasco, V. J. Herrero, V. S. Rábanos, and M. H. Alexander, J. Chem. Phys. **119**, 5860 (2003).

[21]C. J. Eyles, M. Brouard, H. Chadwick, F. J. Aoiz, J. Kłos, A. Gijsbertsen, X. Zhang, and S. Stolte, Phys. Chem. Chem. Phys. **14**, 5420 (2012).

[22]S. F. Boys and F. Bernardi, Mol. Phys. **19**, 553 (1970).

[23]MOLPRO is a package of *ab initio* programs written by H.-J. Werner and P. J. Knowles, with contributions from R. D. Amos, A. Berning, D. L.Cooper, M. J. O. Deegan, A. J. Dobbyn, F. Eckert, C. Hampel, T. Leininger, R. Lindh, A. W. Lloyd, W. Meyer, M. E. Mura, A. Nicklaß, P.Palmieri, K. Peterson, R. Pitzer, P. Pulay, G. Rauhut, M. Schütz, H. Stoll, A. J. Stone and T. Thorsteinsson.

[24]K. P. Huber and G. Herzberg, *Molecular Spectra and Molecular Structure. IV. Constants of Diatomic Molecules* (Van Nostrand Reinhold, New York, 1979).

[25]T. H. Dunning, J. Chem. Phys. **90**, 1007 (1989).

[26]R. A. Kendall, T. H. Dunning, and R. J. Harrison, J. Chem. Phys. **96**, 6796 (1992).

[27]F. M. Tao and Y. K. Pan, J. Chem. Phys. **97**, 4989 (1992).

[28]P. J. Knowles, C. Hampel, and H.-J. Werner, J. Chem. Phys. **99**, 5219 (1993).

[29]P. J. Knowles, C. Hampel, and H.-J. Werner, J. Chem. Phys. **112**, E3106 (2000).

[30]M. Alexander, Chem. Phys. **92**, 337 (1985).

[31]A. R. Edmonds, *Angular Momentum in Qunatum Mechanics* (Princeton, Pircenton, New Jersey, 1974).

[32]R. N. Zare, *Angular Momentum* (Wiley, New York, 1988).

[33]M. Alexander, J. Chem. Phys. **76**, 5974 (1982).

[34]A. D. Esposti and H.-J. Werner, J. Chem. Phys. **93**, 3351 (1990).

[35]G. C. Nielson, G. A. Parker, and R. T. Pack, J. Chem. Phys. **64**, 2055 (1976).

[36]HIBRIDON is a package of programs for the time-independent quantum treatment of inelastic collisions and photodissociation written by M. H. Alexander, D. Manolopoulos, H.-J. Werner, and B. Follmeg, with contributions by P. Vohralik, G. Corey, B. Johnson, T. Orlikowski, P. Valiron and J. Kłos.

[37]I. P. Hamilton and J. C. Light, J. Chem. Phys. **84**, 306 (1986).

[38]S. D. Gamblin, S. E. Daire, J. Lozeille, and T. G. Wright, Chem. Phys. Lett. **325**, 232 (2000).

[39]H. Meyer, J. Kłos, and M. H. Alexander, (2012), to be published.

[40]F. J. Aoiz, J. E. Verdasco, M. Brouard, J. Kłos, S. Marinakis, and S. Stolte, The Journal of Physical Chemistry A **113**, 14636 (2009).

[41]R. A. LaBudde and R. B. Bernstein, J. Chem. Phys. **55**, 5499 (1971).

[42]F. J. Aoiz, V. Sáez-Rabanos, B. Martínez-Haya, and T. González-Lezana, J. Chem. Phys. **123**, 094101 (2005).

[43]M. Alagia, N. Balucani, and L. Cartechini *et al.*, Phys. Chem. Chem. Phys. **2**, 599 (2000).

[44]A. M. Arthurs and A. Dalgarno, Proc. R. Soc. London, Ser. A **256**, 540 (1960).

[45]D. E. Manolopoulos, J. Chem. Phys. **85**, 6425 (1986).

[46]M. H. Alexander and D. E. Manolopoulos, J. Chem. Phys. **86**, 2044 (1987).

[47]C. W. McCurdy and W. H. Miller, J. Chem. Phys. **67**, 463 (1977).

[48]J. J. C. Barrett, H. R. Mayne, and M. Keil, J. Chem. Phys. **100**, 304 (1994).

[49]L. J. Rawluk, M. Keil, M. Alexander, H. R. Mayne, and J. J. V. Barrett, Chem. Phys. Lett. **202**, 291 (1993).

[50]L. González-Sánchez, J. Aldegunde, P. G. Jambrina, and F. J. Aoiz, J. Chem. Phys. **135**, 064301 (2011).

[51]J. Aldegunde, F. J. Aoiz, L. González-Sánchez, P. G. Jambrina, M. P. de Miranda, and V. Sáez-Rábanos, Phys. Chem. Chem. Phys. **14**, 2911 (2012).

[52]J. Kłos, F. J. Aoiz, J. E. Verdasco, M. Brouard, S. Marinakis, and S. Stolte, J. Chem. Phys. **127**, 031102 (2007).

TABLE I. Dispersion coefficients, $C_{n,l}$, of the $V_{\rm sum}$ diabat of the Xe-NO($X^2\Pi$) complex in units of $E_h a_0^n$.

(n,l)	$C_{n,l}$, This work	Nielson *et al.* Ref.[35]
(6,0)	134	170±31
(6,2)	14.6	24.4±8

TABLE II. The interaction energies at the stationary points of adiabatic A' and A'' surfaces, and the diabatic $V_{\rm sum}$ surface.

PES	Configuration	$D_{\rm e}/{\rm cm}^{-1}$
A'	Xe$\cdots$N-O, $\gamma = 0°$, $R = 8.73\,{\rm a}_0$	104.49
A'	Xe$\cdots$O-N, $\gamma = 180°$, $R = 8.37\,{\rm a}_0$	107.23
A'	$R_{\rm e} = 7.46\,{\rm a}_0$, $\gamma_{\rm e} = 94°$	148.68
A''	$R_{\rm e} = 7.68\,{\rm a}_0$, $\gamma_{\rm e} = 64°$	148.23
$V_{\rm sum}$	$R_{\rm e} = 7.52\,{\rm a}_0$, $\gamma_{\rm e} = 90°$	141.70

TABLE III. Selected bound states (up to energy of -68 cm^{-1}) of Xe-NO($X^2\Pi$) complex for $J = \frac{1}{2}$ up to $\frac{3}{2}$. Energies are in cm^{-1} relative to the energy of the separated monomers. n_s and n_b specify the number of nodes in the van der Waals stretching and bending modes of the complex, respectively. The P quantum number denotes the projection of the total angular momentum J on the z-axis of the molecular frame. The + and − signs denote the total parity p.

(n_s, n_b)	P	$J = \frac{1}{2}+$	$J = \frac{1}{2}-$	(n_s, n_b)	P	$J = \frac{3}{2}+$	$J = \frac{3}{2}-$
(0,0)	1/2	-116.927	-116.884	(0,0)	1/2	-116.828	-116.768
(0,0)	1/2	-116.814	-116.859	(0,0)	1/2	-116.667	-116.731
(0,1)	1/2	-100.125	-100.099	(0,1)	3/2	-113.244	-113.244
(0,1)	1/2	-99.678	-99.713	(0,1)	3/2	-113.058	-113.058
(1,0)	1/2	-95.421	-95.425	(1,0)	1/2	-100.031	-99.981
(1,0)	1/2	-94.307	-94.307	(1,0)	1/2	-99.538	-99.605
(0,2)	1/2	-87.557	-87.558	(0,2)	3/2	-95.409	-95.404
(0,2)	1/2	-86.098	-86.098	(0,2)	1/2	-95.307	-95.322
(1,1)	1/2	-82.469	-82.475	(1,1)	3/2	-94.256	-94.250
(1,1)	1/2	-80.274	-80.279	(1,1)	1/2	-94.176	-94.183
(1,2)	1/2	-74.817	-74.923	(2,0)	3/2	-90.180	-90.180
(1,2)	1/2	-74.604	-74.502	(2,0)	3/2	-88.721	-88.721
(2,1)	1/2	-71.026	-71.034	(0,3)	1/2	-87.449	-87.451
(2,1)	1/2	-68.726	-68.722	(0,3)	1/2	-85.987	-85.985

TABLE IV. Integral cross sections obtained from the o–s QM, c–s QM and QCT scattering calculations for $E_{col} = 63\,meV$ with respect to the initial state with $j = 1/2$, $\Omega = 1/2$, $\epsilon = e(+1)$ or $\epsilon = f(-1)$ ($j = 0$ in case of the closed shell and QCT approach). The SO-conserving ($F_1 \rightarrow F_1$) and SO-changing ($F_1 \rightarrow F_2$) o–s QM cross sections are given resolved for initial and final Λ-doublets and also summed over final and averaged over initial Λ-doublet and summed over final Ω' ($\Delta\Omega = 0 + \Delta\Omega = 1$ column). Cross sections are in units of $Å^2$.

	Final state		ϵ			ϵ		$\Delta\Omega = 0 + \Delta\Omega = 1$	Closed shell	
	Δj	ϵ'	e	f		e	f	o–s QM	QCT	c–s QM
$F_1 \rightarrow F_1$	0	f	3.89	290	$F_1 \rightarrow F_2$	–	–	3.89	–	–
		e	291.0	3.89						
	1	f	8.19	8.02		1.24	0.27	17.9	31.1	11.6
		e	8.01	8.45		0.29	1.25			
	2	f	2.63	12.3		0.26	0.66	16.2	17.3	22.9
		e	12.5	2.64		1.12	0.25			
	3	f	4.83	3.42		1.34	0.13	10.0	11.9	6.78
		e	3.41	4.90		0.15	1.86			
	4	f	1.42	6.09		0.13	0.83	8.64	9.23	11.8
		e	5.68	1.44		1.54	0.15			
	5	f	3.88	1.25		1.14	0.10	6.49	6.77	3.98
		e	1.28	3.35		0.13	1.86			
	6	f	1.20	4.22		0.11	0.60	6.04	5.57	6.90
		e	3.30	1.26		1.20	0.19			
	7	f	2.90	1.18		0.57	0.12	4.59	4.83	4.46
		e	1.16	1.98		0.20	1.08			
	8	f	1.16	2.81		0.16	0.22	3.97	3.95	3.46
		e	1.79	1.04		0.47	0.30			
	9	f	1.86	1.17		0.15	0.15	2.95	3.32	4.50
		e	0.97	1.00		0.28	0.31			
	10	f	1.12	1.40		0.12	0.06	2.31	2.76	1.52
		e	0.75	0.78		0.12	0.28			

FIG. 1. Radial $V_{lm}(R)$ expansion coefficients of the a) $V_{\rm sum}$ and b) $V_{\rm diff}$ diabats, respectively.

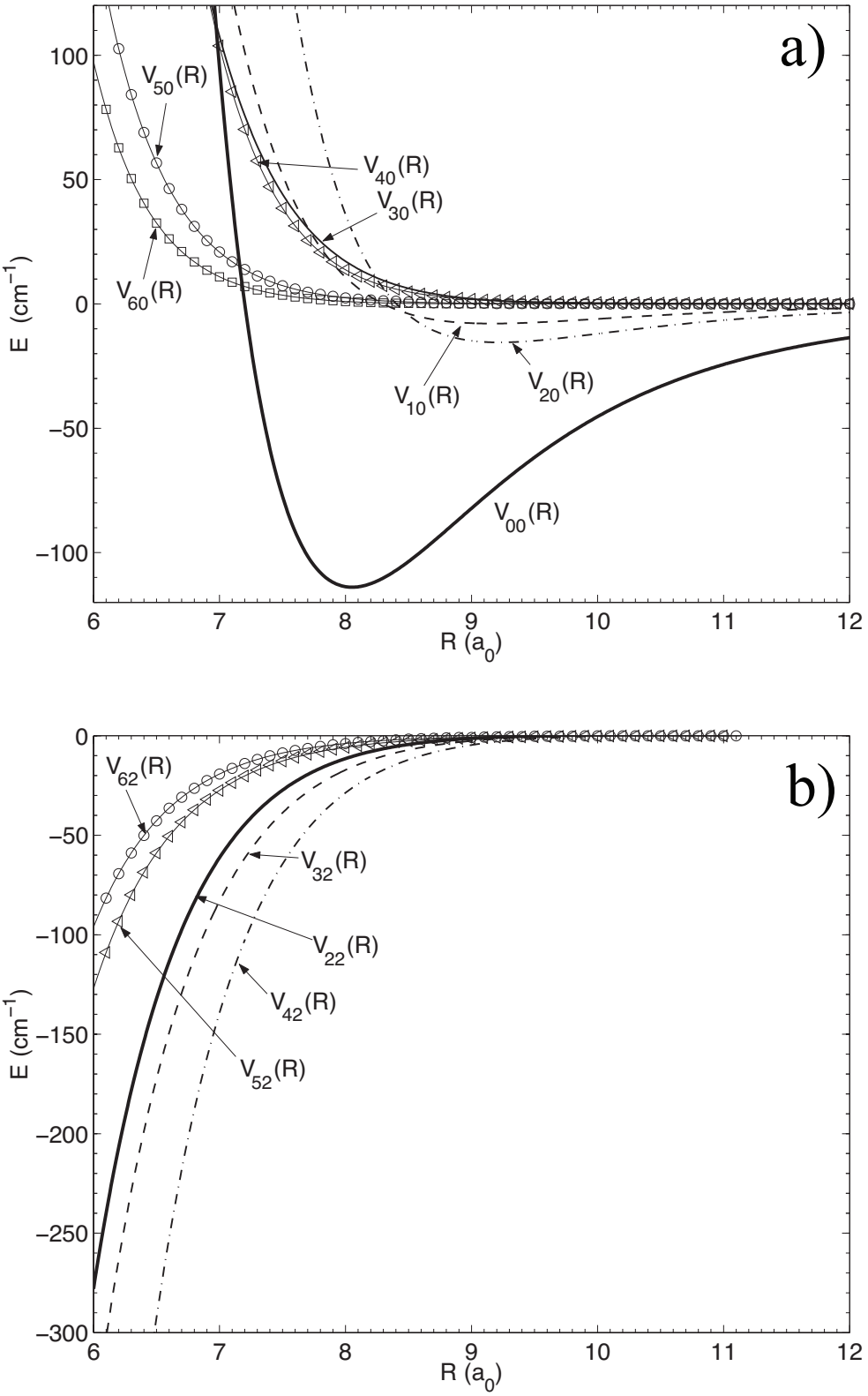

FIG. 2. (Color online) Contour plots of the adiabatic surfaces, a) A' and b) A''. Energy in cm^{-1}. γ=0° corresponds to the linear Xe–N–O configuration. The contour corresponding to 508 cm^{-1} represents that of the collision energy of 63 meV. Negative energy contours, dashed (blue) line; positive energy contours, solid (red) line.

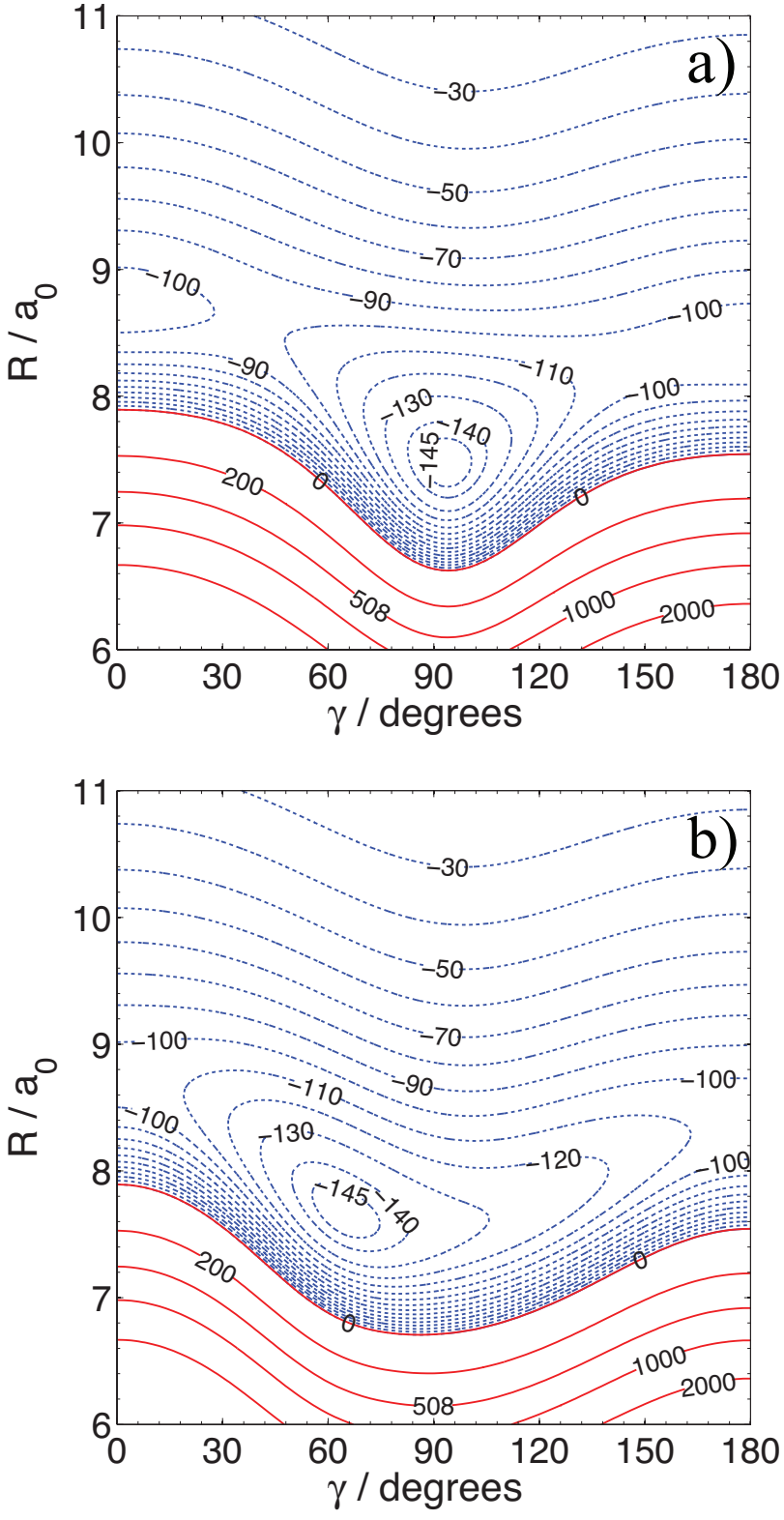

FIG. 3. (Color online) Contour plots of the diabatic surfaces, a) $V_{\rm sum}$ and b) $V_{\rm diff}$. Energy in $\rm cm^{-1}$. γ=0° corresponds to the linear Xe–N–O configuration. The contour corresponding to 508 $\rm cm^{-1}$ represents the collision energy of 63 meV. Contours as in Fig. 2

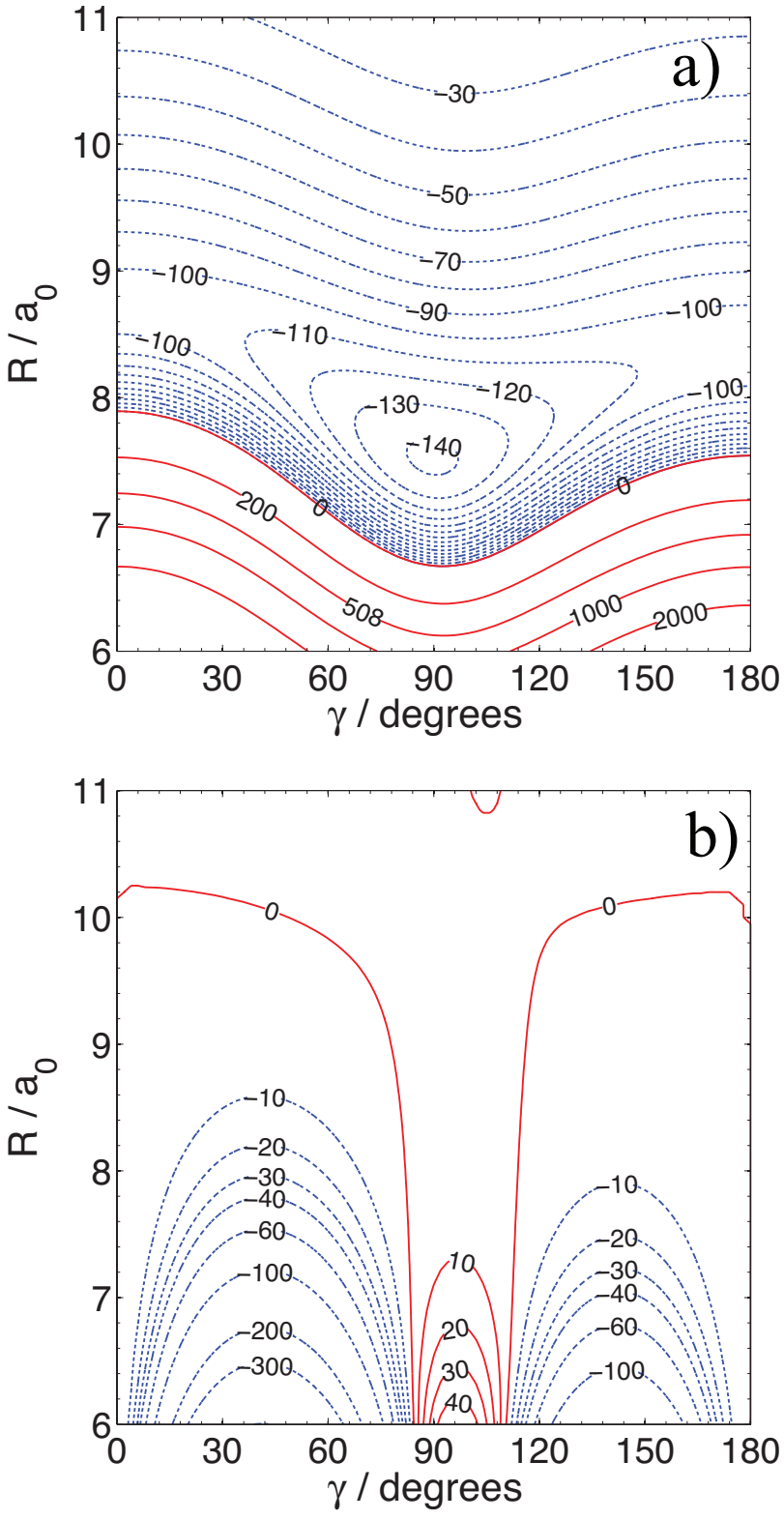

FIG. 4. (Color online) Integral cross sections at $E_{\rm col} = 63\,$meV for rotational transitions from the initial $j = 0.5$ and Ω=1/2 NO rotational state. Open squares and solid (blue) line, o–s QM data; open circles and dot–dash (black) line, c–s QM data; filled circles and dashed (red) line, QCT results. The o–s QM results are summed over final Λ-doublet and Ω states and averaged over initial Λ-doublet levels.

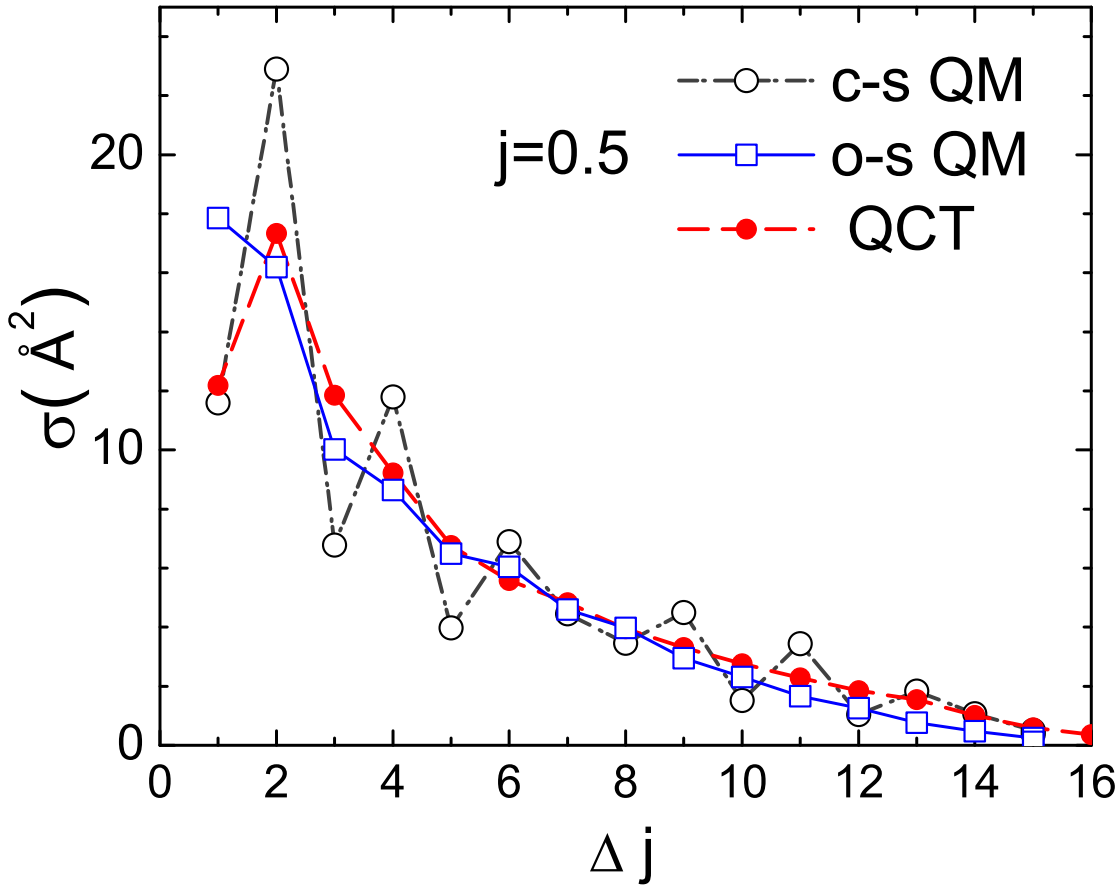

FIG. 5. (Colour online) Open–shell QM integral cross sections at $E_{\rm col}$ = 63 meV from j=0.5, Ω=1/2, and $\epsilon = +1$ (e) initial state into the Ω=1/2, F_1 (upper panel) and Ω=3/2, F_2 (lower panel) manifolds. Open (blue) circles $e \rightarrow e$ transitions; filled (red) circles $e \rightarrow f$ transitions.

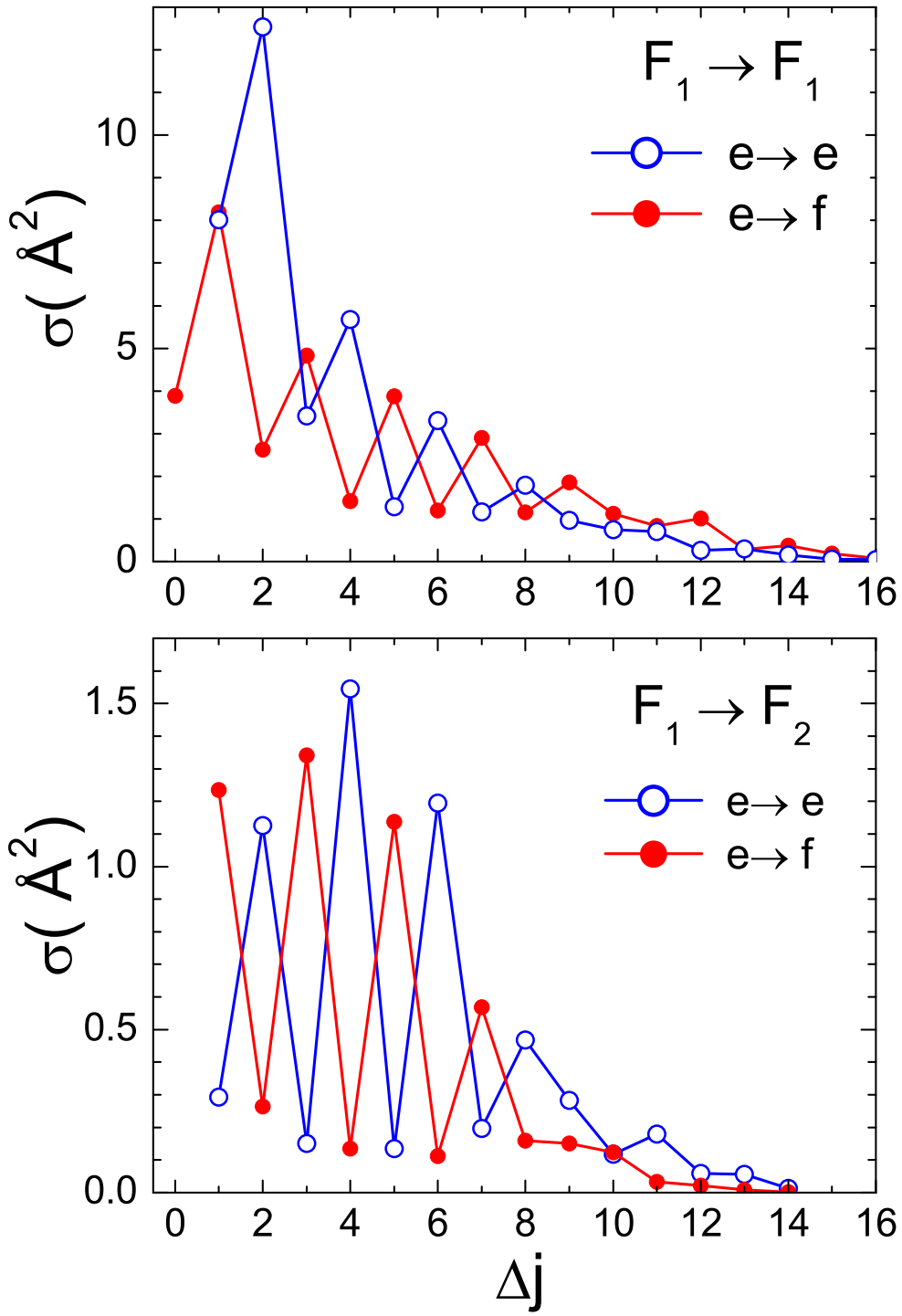

FIG. 6. Integral cross sections for collision energy $E_{\rm col} = 63$ meV from the initial rotational states: a): $j = 2.5$, b) $j = 5.5$, c)$j = 8.5$ and d)$j = 14.5$ (j=0, 2, 8 and 14, respectively, for c–s calculations). The QM o-s results are summed over final Λ-doublet and Ω states and averaged over initial Λ-doublet levels. Lines and symbols as in Fig. 4.

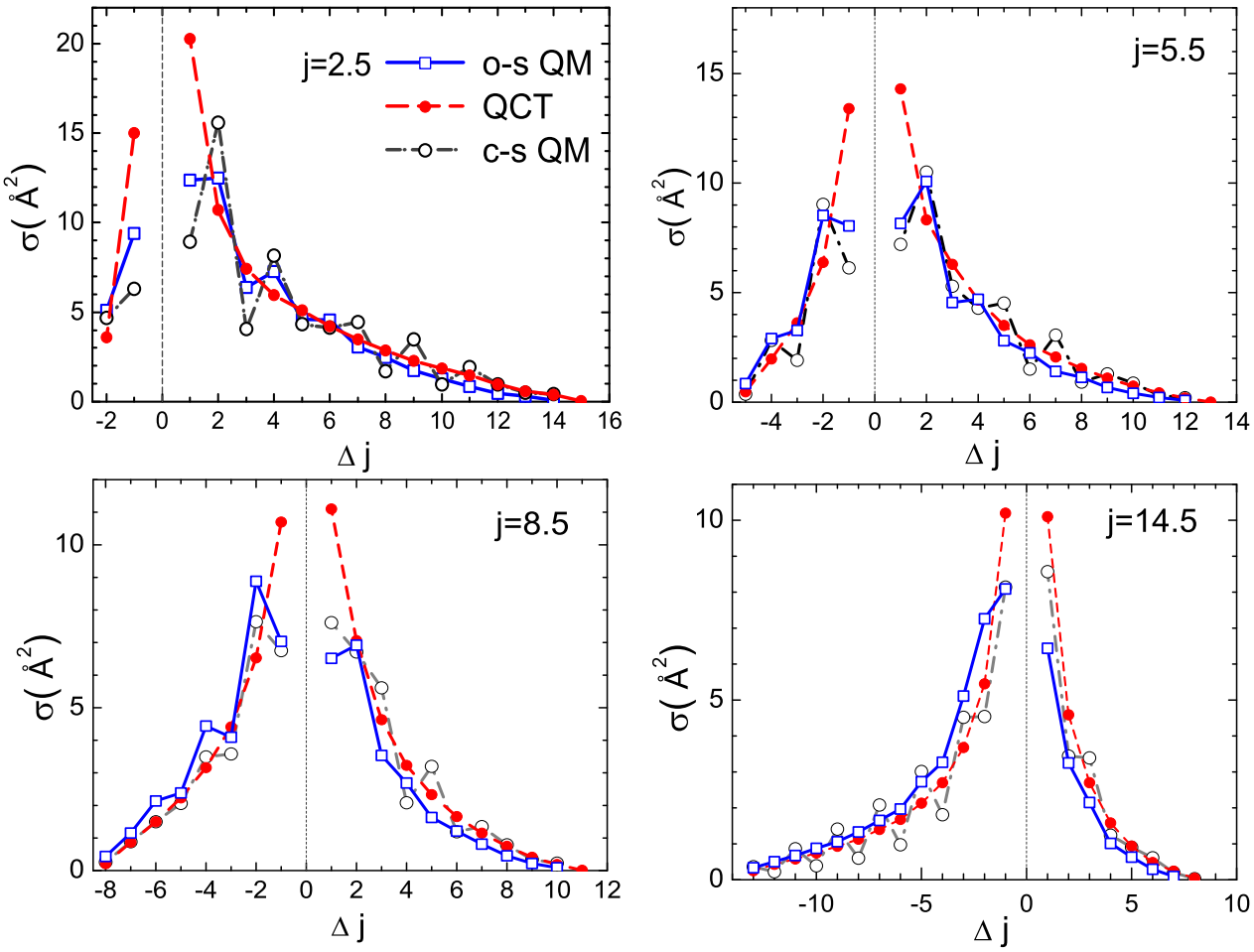

FIG. 7. Top panel: Total opacity functions, $P(J; j = 0.5)$, from QCT (dashed, red line), open-shell QM (solid, blue line) and closed-shell QM (dot–dashed, black line) calculations for $E_{\rm col} = 63\,{\rm meV}$ for initial rotational state Ω=1/2, $j = 0.5$ (j=0 for c–s calculations). Bottom panel: Total (summed over final rotational states) opacity functions from the o–s QM calculations resolved for the final spin-orbit manifold with $\Omega' = 1/2$ (F_1) and $\Omega' = 3/2$ (F_2), respectively. They sum up to form a red dashed line representing the total o–s QM $P(J)$. The upper x axes show the corresponding values of the impact parameter, $b = [\ell(\ell+1)]^{1/2}/k$, where $k = (2\mu E_{\rm coll})^{1/2}/\hbar$.

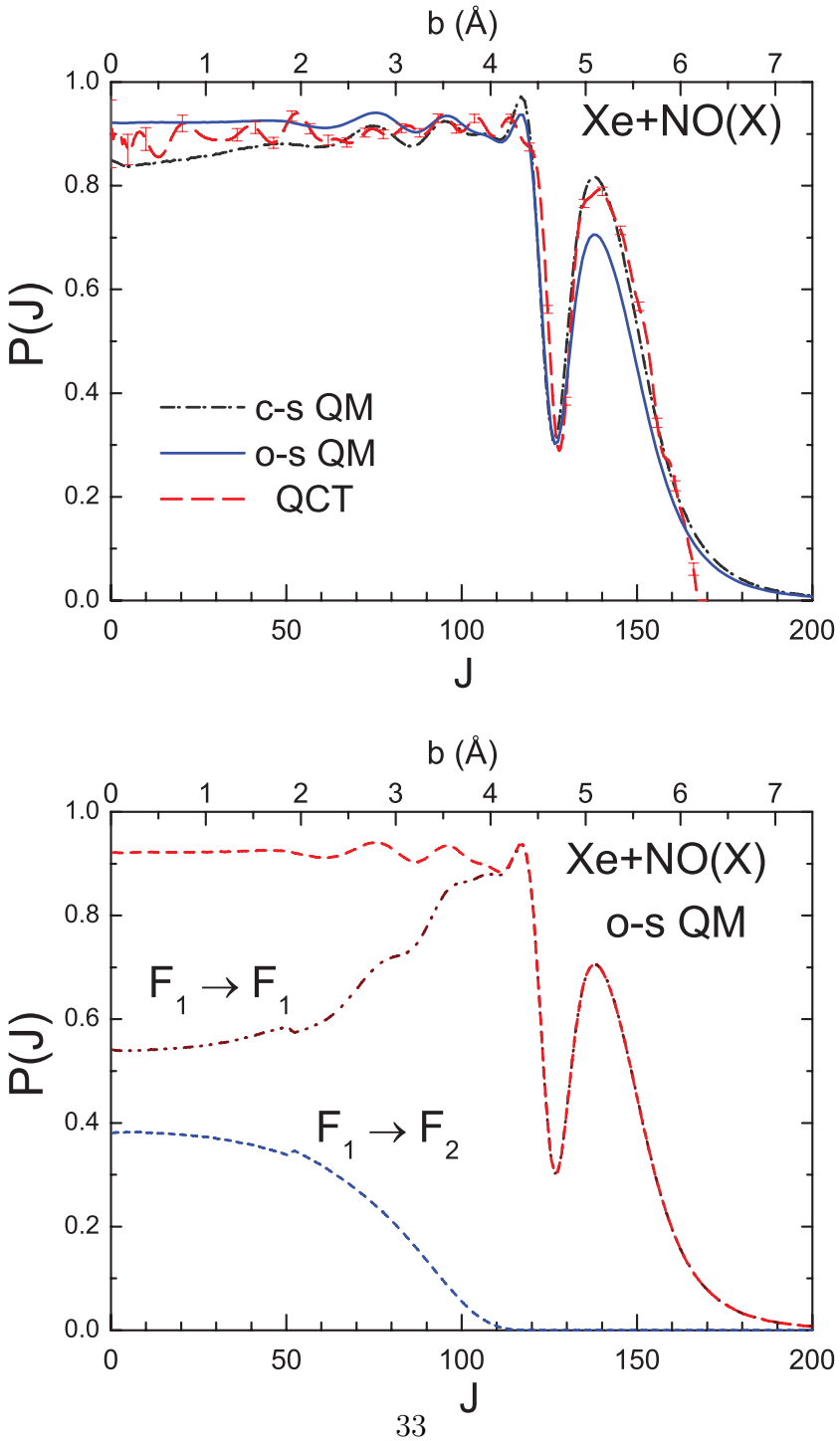

FIG. 8. Rotationally state resolved opacity functions, $P(J; j = 0 \rightarrow j')$, from closed-shell QM calculations for $E_{\rm col} = 63\,{\rm meV}$ for various odd Δj transitions. The arrows in each panel indicate the J value of the *glory* associated to the L-type rainbow; all of them correspond to a value of J=123. As can be seen, for $\Delta j > 5$ the bulge associated with the rainbow scattering is absent.

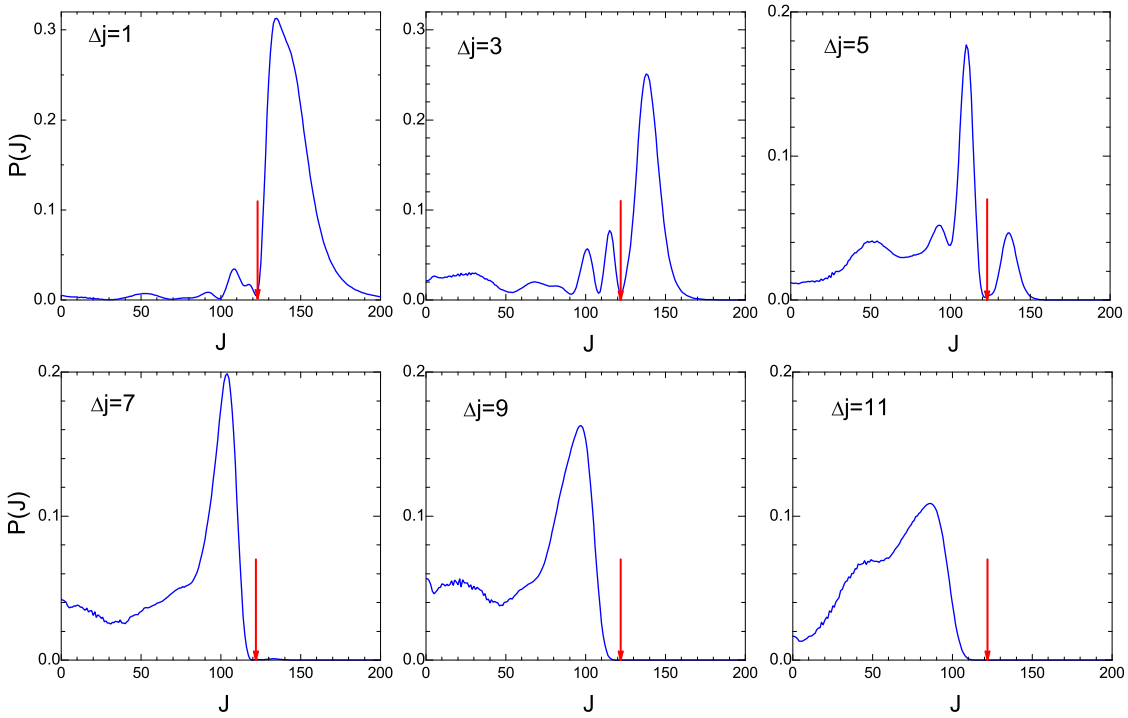

FIG. 9. Total opacity functions from the closed-shell QM calculations at collision energy $E_{\mathrm{col}} = 63\,\mathrm{meV}$ for the initial rotational state $j = 0$ for the series of Rg-NO(X) systems.

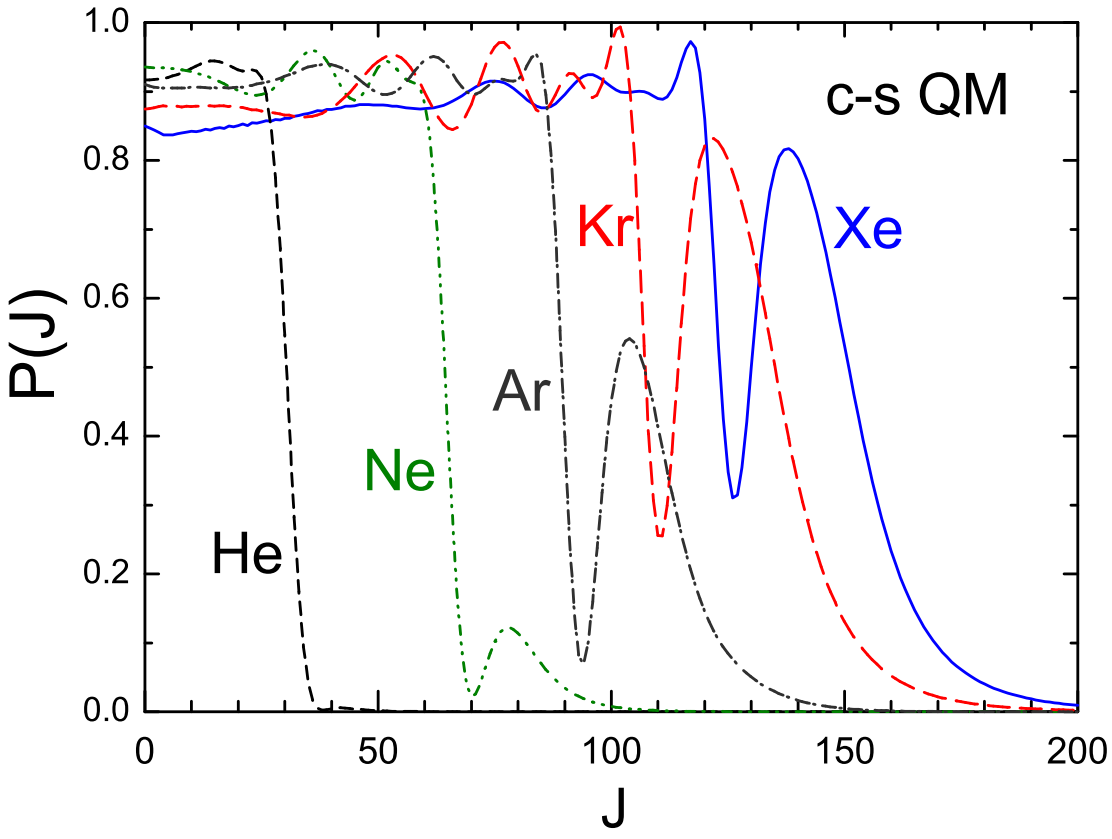

FIG. 10. Total opacity $P(J;j)$ functions from the QCT (top panel), open-shell QM, o–s, (middle panel) and closed-shell c–s QM (bottom panel) calculations for $E_{\rm col} = 63\,{\rm meV}$ as a function of initial rotational state j. The o-s results are averaged and summed over the two initial and final, respectively, lambda doublet components transitions and summed over $F_1 \rightarrow F_1$ and $F_1 \rightarrow F_2$ transitions.

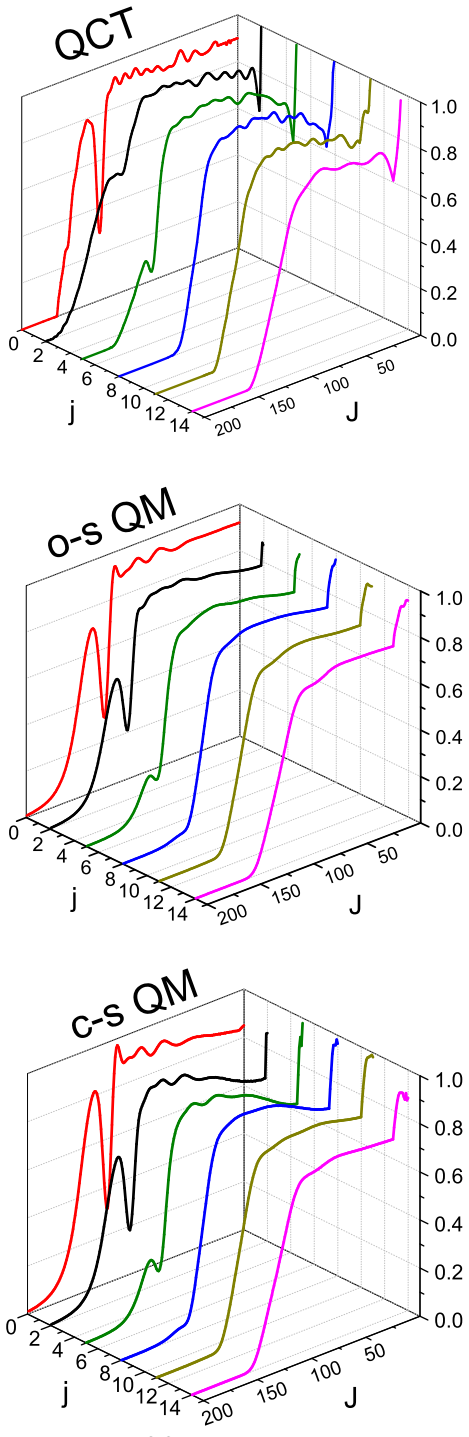

FIG. 11. Panel (a): Classical deflection function (scattering angle *vs.* impact parameter) for rotationally inelastic scattering of NO in its ground state (j=0) with Xe at 63 meV collision energy. Deflection angles above the glory impact parameter (≈ 4.2 Å) are negative, corresponding to far-side collisions. The top x axis shows the values of the orbital angular momentum. Panel (b): Total differential cross sections from the QCT, o–s QM, and c–s QM calculations at $E_{\rm col} = 63$ meV for initial rotational state $j = 0.5$ (j=0 for c–s calculations). The o–s QM DCS is summed over all final states and averaged over initial fine states. Lines as in Fig. 10.

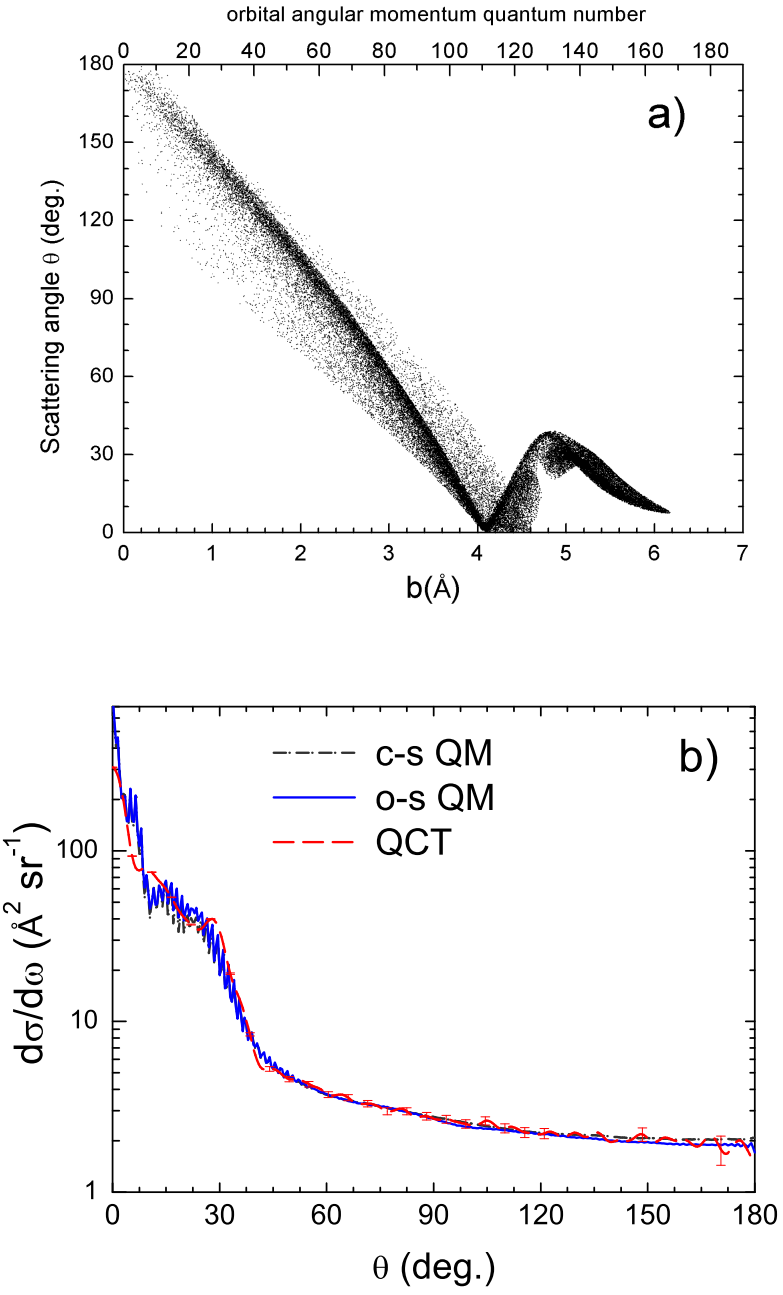

FIG. 12. State–to–state angular distributions, $2\pi \sin\theta d\sigma/d\omega$, for selected transitions out of the initial $j = 0.5$ rotational level from the QCT and o–s QM calculations at $E_{\rm col} = 63\,{\rm meV}$. The o–s QM DCSs are summed over Ω=1/2, 3/2 and e and f final states and averaged over initial e and f states. Solid (blue) line, o–s QM data; dashed (red) line, QCT data.

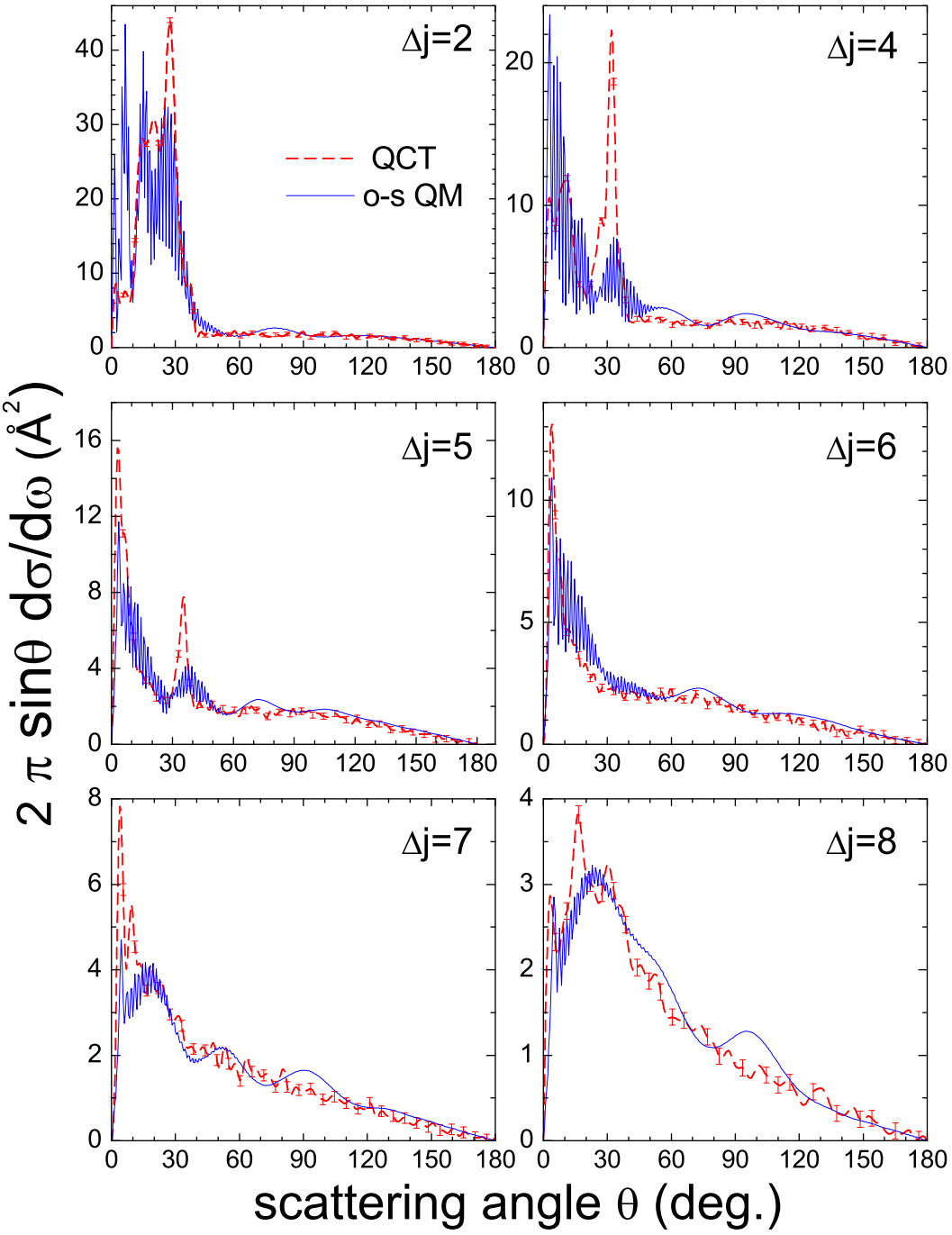

FIG. 13. Same as Fig. 12 but out of the initial $j = 14.5$ rotational level at a collision energy of $E_{\rm col} = 63\,{\rm meV}$.

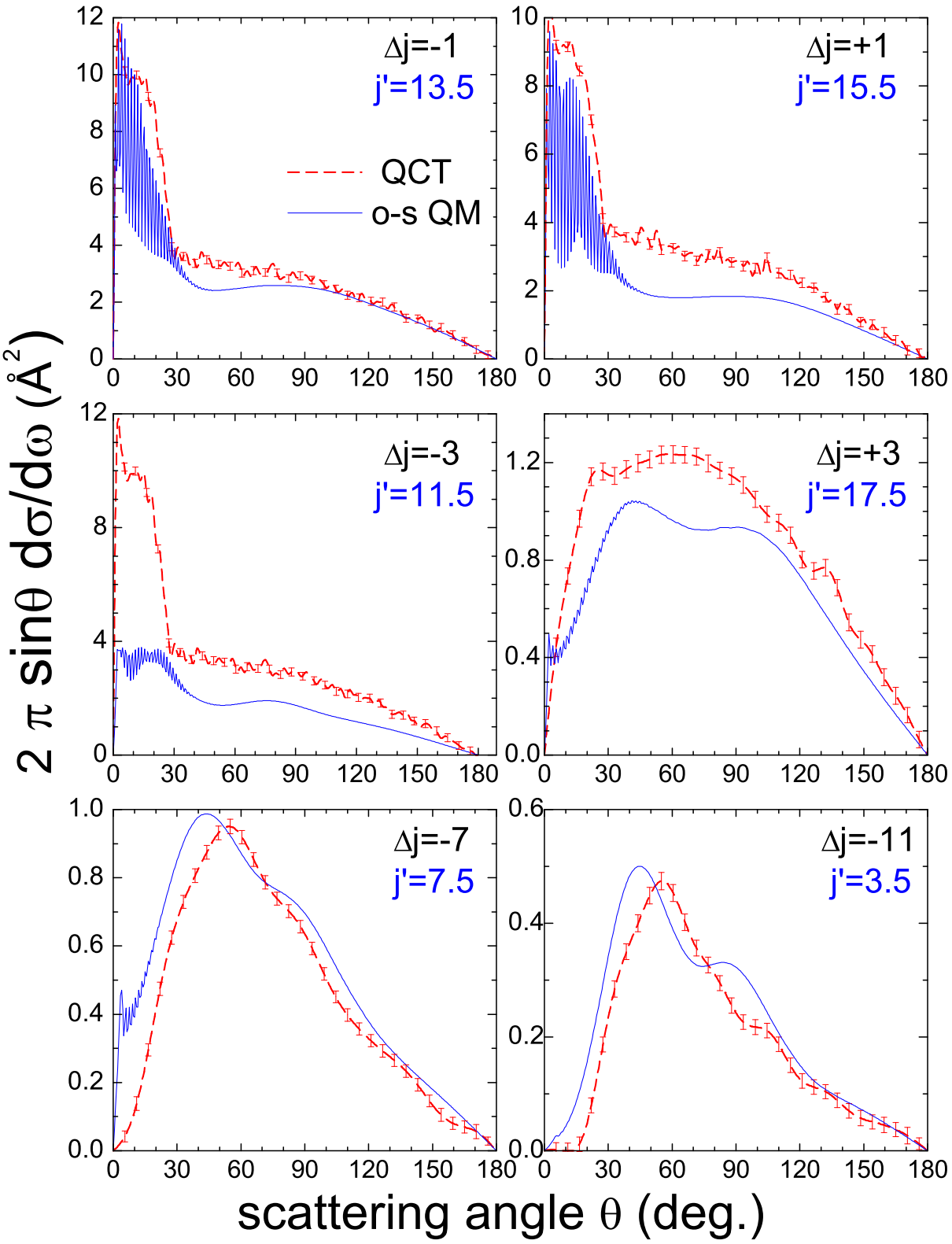

FIG. 14. o–s QM DCS for selected transitions out of the initial $j = 0.5$ rotational level and selected Λ–doublet components at $E_{\rm col} = 63\,$meV. The left and right columns display the parity breaking and parity conserving transitions, respectively.